Sensors & Actuators: B. Chemical 409 (2024) 135592

Contents lists available at ScienceDirect

Sensors and Actuators: B. Chemical

journal homepage: www.elsevier.com/locate/snb

Developing a nanomaterial-based 3D-printed platform: Application as a cancer aptasensor via detection of heat shock protein 90 (HSP90)

Masoud Negahdary [a,*], Claudimir Lucio do Lago [a], Ivano Gebhardt Rolf Gutz [a], Rafael Martos Buoro [b], Michelangelo Durazzo [c], L.úcio Angnes [a,*]

[a] Department of Fundamental Chemistry, Institute of Chemistry, University of São Paulo, Av. Prof. Lineu Prestes, 748, São Paulo 05508-000, Brazil
[b] Institute of Chemistry of São Carlos, University of São Paulo, Av. Trabalhador São-Carlense, 400, São Carlos 13556-590, Brazil
[c] Nuclear and Energy Research Institute, National Commission of Nuclear Energy (IPEN/CNEN - SP), São Paulo, SP 05508-000, Brazil

ARTICLE INFO

Keywords:
Heat shock protein 90 (HSP90)
Cancer biomarker
Electrochemical aptasensor
3D-printed electrode
Graphene oxide (GO)
Frost-like gold nanocrystals (FGNCs)

ABSTRACT

Overexpressed heat shock protein 90 (HSP90) has been proven as a new cancer biomarker, and its detection can be used as an auxiliary diagnosis. In this research, we designed an electrochemical aptasensor to detect this biomarker. Initially, a 3D-printed electrode was designed and produced while the electrode surface (made from a conductive carbon black/ polylactic acid (CB-PLA) filament) was improved by CO_2 laser ablation. Then, the electrode surface was modified with graphene oxide (GO) and an array of frost-like gold nanocrystals (FGNCs); the results showed that the final surface covered with gold contained nano/microstructures with a mean width of ~ 65 nm and a mean length of ~ 509 nm. Also, a significant increase in the electrochemically active surface area was observed for modified surfaces with GO and FGNCs. Efficient immobilization of aptamer strands on the gold surface could complete the assembly of this aptasensing platform, which could detect analyte molecules in a linear range from 0.1 to 200 ng mL^{-1}. The estimated limit of detection (LOD) and the limit of quantification (LOQ) were as low as 0.1 ng mL^{-1} and 0.23 ng mL^{-1}, respectively. The performance of reproducibility (5 times), regeneration (5 times), and stability (7 days) were satisfactory (low relative standard deviation (RSD)). Also, this aptasensor showed adequate performance for selective and accurate analyte capturing in the presence of interfering agents and spiked analyte concentrations in serum samples.

1. Introduction

The early detection of cancer significantly enhances the possibilities of successful control while enabling the adoption of more potent treatment approaches [1,2]. The assay of biomarkers in biofluids can supply early diagnosis and rapid directing treatment when the cancer is still in its early stages [3]. Also, measuring biomarkers can be helpful in follow-up and evaluating anti-tumor immune responses (prognosis) [4,5]. Changes in biomarker levels may indicate cancer regression, recurrence, or response to treatment [1,3]. The advantages of using biomarkers to diagnose cancer include not needing invasive processes such as biopsy and surgery and reducing cost and time compared to other methods [6–8]. Nevertheless, diagnosing cancer using only biomarkers is insufficient and requires additional evaluations such as medical imaging and histological examination [9,10].

Heat shock protein 90 (HSP90) is present in human cells, and its concentration increases in blood under stress conditions, which plays a vital role in maintaining cell balance and function [11,12]. In cancer cells, HSP90 activity is usually increased. This protein can interact with other cancer proteins and support them to be combined and strengthened [13,14]. Indeed, the high level of HSP90 in cancer cells may be due to an enhanced need for this protein to maintain the strength and proper function of cancer proteins [13,15]. Hence, HSP90 has been investigated as a diagnostic biomarker in several cancers, especially ovarian, lung, prostate, and hepatocellular carcinoma [16–23]. Clinical results obtained from more than 500 healthy individuals confirmed that the normal range of HSP90 in the blood is up to 82.06 ng mL^{-1} [24]. It is conceivable that the monitoring of HSP90 levels by minimally invasive tests could allow for the evaluation of the progress of the cancer. Most importantly, HSP90 inhibitors under development might be beneficial for patients with cancers that present with overexpression of HSP90 [25]. Approaches such as ELISA, immunohistochemistry, and western blotting are commonly used for quantifying HSP90 in biological samples derived from cancer [26–28]. However, not all forms of antibodies may

* Corresponding authors.
E-mail addresses: mnegahdary@tamu.edu (M. Negahdary), luangnes@iq.usp.br (L.úcio Angnes).

https://doi.org/10.1016/j.snb.2024.135592
Received 6 December 2023; Received in revised form 28 February 2024; Accepted 3 March 2024
Available online 4 March 2024

be suitable for such assays. Moreover, subjective analysis of results and deciding what the numerical values mean requires deep expertise. For example, in Western blotting, the specific condition necessary for the procedure makes the signal intensity of the band variable, which inevitably affects the quantification. Interestingly, the number of HSP90 in a cell and the amount of HSP90 in tissue may not correlate at all.

Compared to other biomarker detection methods, electrochemical aptasensors work based on molecular interactions between aptamers (as specific and high-stable biorecognition elements) and the surface of working electrodes assembled to detect biomarkers [29–33]. These short sequences are usually composed of ≤100 nucleotides, selected through a systematic evolution of ligands by exponential enrichment (SELEX) [34–36]. The advantages of electrochemical aptasensors include high sensitivity, fast response time, selectivity, stability and reproducibility, integration capability, and lower cost than other diagnostic methods [30,33,37,38]. For instance, 3D-printed electrodes have many advantages and capabilities that make them suitable for developing a new generation of electrochemical biosensors [39–42]. 3D-printing technology can produce electrodes with the desired shape and size [43–45]. This technology is faster, easier, and more controllable than traditional methods of producing electrodes, and these advances reduce costs and production time and increase reproducibility [46,47]. 3D-printed electrodes can be made from various materials such as polymers, composites, and conductive materials and are designed with desired mechanical, electrochemical, and physical properties or integration between all [47–49]. In addition, these electrodes can accurately measure biomarkers due to their specific design and flexible fabrication capabilities [39,49,50].

Surface modification of 3D-printed electrodes using nanomaterials such as graphene oxide (GO) and gold has many advantages [39,51,52]. The presence of these biocompatible nanomaterials on the surface of electrodes increases the electroactive surface area, which gives signal amplification and, subsequently, more sensitivity and accuracy in detecting analytes [29,39,53,54]. Also, these nanomaterials (GO/gold-based) improve the strength and stability of electrodes and make them more resistant to possible damage from chemicals and external environments. Considering innovations, specific architecture, and advantages of 3D-printed electrodes, there is no report about developing aptasensors for cancer diagnosis based on these types of electrodes.

Here, we designed and developed a new carbon-based 3D-printed electrode with improvements in the manufacturing process, including the use of an independent dual extrusion (IDEX) printer, allowing sequential printing of the conductive electrode and the isolating body with an embedded copper wire terminal to minimize the electrical resistance of the connection with the potentiostat. In order to achieve the desired final bare 3D-printed electrode surface, a CO_2-based laser-ablation process was performed after printing. Then, to improve the hydrophilicity of the electrode surface in the electrolyte, the surface was treated with ethanol. Afterward, the electrode surface was modified with GO (via drop-casting) and FGNCs (via electrodeposition). In the next step, the accessible electrode surface containing widely distributed FGNCs was employed as an optimum substrate for immobilization (through interaction between thiol and gold) of thiol-functionalized aptamer strands with high affinity against capturing HSP90 molecules. This aptasensor provided a new and low-cost quantitative method for detecting this cancer biomarker, as demonstrated.

2. Materials and methods

All employed materials, reagents, instruments, and relevant methods are presented in detail in the Supplementary Material.

2.1. Architecture of the 3D-printed electrode and principle of detection

Initially, a new 3D-printed electrode was designed and produced. Here, two different filaments were used: one of them was conductive and employed to print the working electrode circular area, and the other one was a non-conductive filament used to print the body of the electrode (Figs. 1A, S1A, B). An IDEX printer has proven to be particularly suitable, as it meets the need to switch seamlessly between two materials with different characteristics. Although this printing process helps to solve the problem of having two different materials, the problem of the electric contact remains because the electric resistivity of the conductive part (CB-PLA) is significantly high (1.15 Ω·m). The previous solution adopted used a stainless-steel screw as the external electrical contact to the electrode [39,51]. Here, the printing process contains two separate steps. In the first step, a channel was also printed, which was then used to install a copper wire (0.5 mm) as the electrode contact. Afterward, the second step of printing was executed (Table S1), thus completing the electrode production (Fig. 1A). The use of the copper wire with a ring-shaped end embedded in the printed electrode in this design was advantageous and intriguing because two aspects: 1) low electrical resistivity of this metal ($1.68\ 10^{-8}$ Ω·m), which provided the optimum conducting path from the electrode to the external electric contact (Figs. 1A, S2A-E), and 2) being flexible, copper wire can be easily shaped to follow any path designed within the electrode body. Taking into account the resistivity of the materials and the sizes of the electrode and the wire connection, the resistance of the conductive CB-PLA is ca. 20, 000 times higher than the copper contact, which suggests that device designs with longer paths for the wire could be considered without significant contribution to the total resistance.

In order to achieve the final bare 3D-printed electrode, several post-production treatments were performed (Fig. 1A). The first step was polishing with different grits of sandpaper to eliminate unwanted materials and reach a smooth surface. Then, the CO_2 laser ablation process was performed to improve the electrochemical property of the electrode by removing excess and inactive layers of the printed conductive polymer [39,55]. Afterward, the electrode surface was washed and dried at 45 °C for 5 min to remove any moisture. In the next step, the surface of the electrode was treated with ethanol and then modified with GO and FGNCs, respectively (Fig. 1B). The ethanol drip on the electrode had three main reasons: 1) Due to its low interfacial tension, it penetrates deeply in the pores and helps to washout possible (hydrophobic) contaminants from the electrode surface; 2) Chemical interaction with the carbon materials of the electrode may promote the formation of some polar functional groups (e.g., OH); and 3) Improve the hydrophilic property of the bare 3D-printed electrode when in contact with the aqueous electrolyte solution, enabling the access of reagents by diffusion and charge transfer kinetics at the electrode-electrolyte interface, thus leading to better overall electrochemical performance.

Then, the surface of the electrode was modified with drop-casted GO and subsequently with electrodeposited FGNCs, as the application of these nanomaterials improved the electrochemical properties of the electrode significantly, as demonstrated in the morphological and electrochemical characterizations presented in Section 3.1.

Subsequently, the assembly of the aptasensor was promoted through the immobilization of 10 μM thiol-functionalized HSP90 RNA aptamer (5'-GGGAGACAAGAAUAAACGCUCAAAU-GAUUGCCCAUUCGGUUAUGCUUGCGCUUCCUAAAGAGCUUCGA-CAGGAGGCUCACAACAGGC-3' [56]) on the electrode surface (Fig. 1C). More details about features of the aptamer used are presented in Table S2. In addition, the secondary structure of employed HSP90 aptamer is represented in Fig. S3A. Thiol molecules joined to the 5' end strongly adsorb on the FGNCs, binding the aptamer strands covalently to the electrode surface. Finally, non-specific aptamer immobilization was blocked by 6-mercapto-1-hexanol (MCH) [57], and a stable and well-organized self-assembled monolayer (SAM) was established on the electrode surface. The KCl-based electrolyte employed in this research contained ferro/ferricyanide ($K_4Fe(CN)_6/K_3Fe(CN)_6$) as the redox marker. The presence of aptamer strands (due to the carrying of negatively-charged phosphate backbone) on the electrode surface

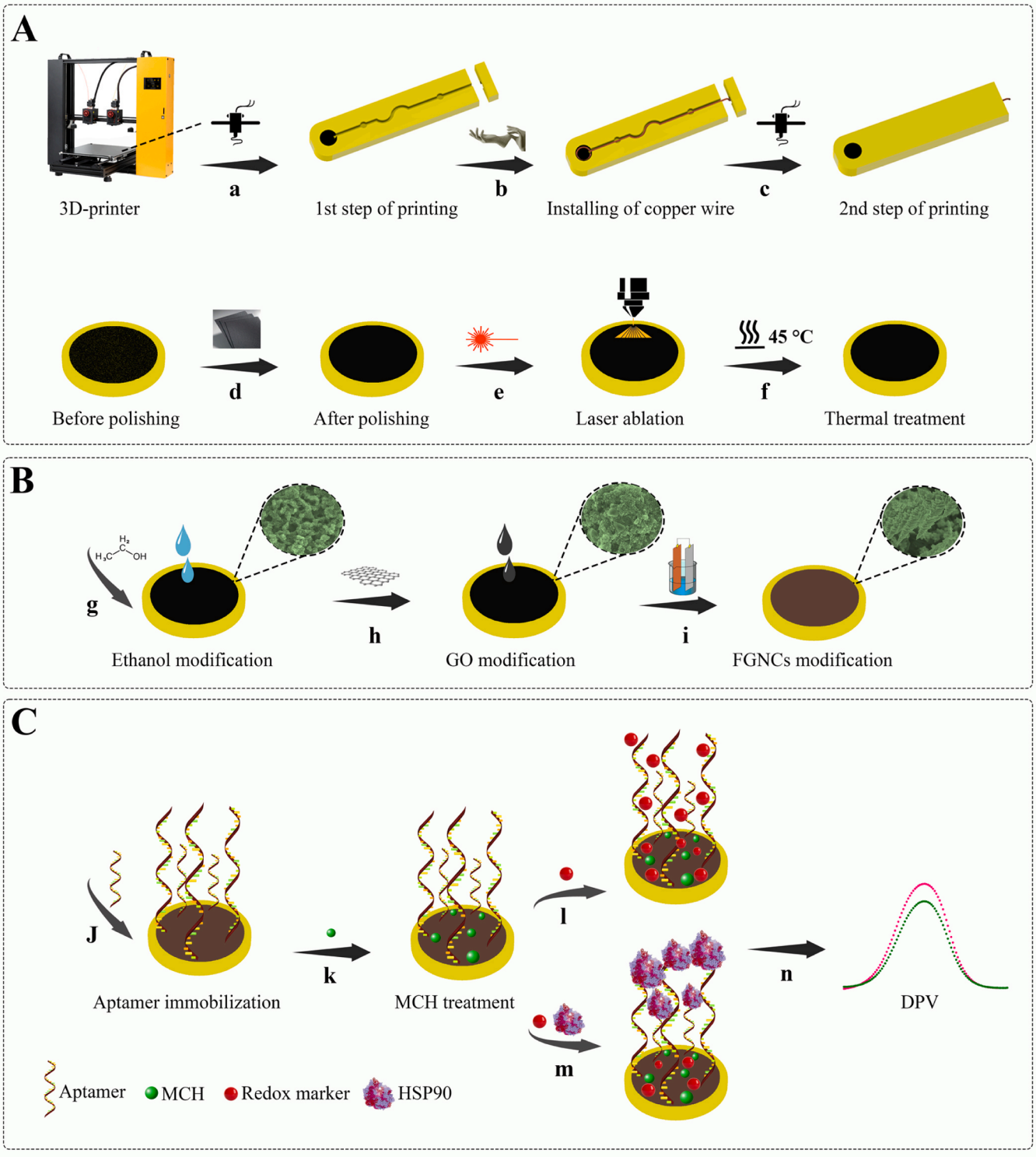

Fig. 1. Designing HSP90 aptasensing platform; ***constructing and post-production treatments for preparation of the final bare 3D-printed electrode*** (**A**): printing the first part of the electrode, containing channel (***a***), temporary stopping the printing process and installing a copper wire as the electrode contact; the extra printed part acted as a holder to keep the copper wire in a fixed position during the printing process (***b***), second step of printing, finalizing the electrode printing (***c***), polishing with different grits sandpapers (***d***), treating the surface by CO_2 laser ablation process (***e***), washing and mild thermal (45 °C) treatment for 5 min (***f***); ***surface modifications*** (**B**): modification with dropped ethanol (***g***), modification with GO through drop-casting (***h***), and modification with an array of FGNCs through electrodeposition (***i***); ***assembly of the aptasensor*** (**C**): immobilization of a thiol-functionalized aptamer on the electrode surface (***j***), treatment with MCH to block unwanted aptamer interactions (***k***), immersing the aptasensor in the electrolyte containing the redox marker (***l***), aptasensor status in the presence of the redox marker and analyte (***m***), and assay the electrochemical responses through DPV (in the absence of the analyte (pink color) and in presence of the analyte (green color)) (***n***).

produces an electrostatic repulsion to the redox marker anions, decreasing DPV peak current compared to the signal recorded before aptamer immobilization. Furthermore, when increasing the concentration of analyte molecules (MW 90-kDa), the accessible areas of the electrode surface are gradually occupied by this protein, restricting the entry of the redox marker ions and consequently attenuating the electron transfer process, resulting in a decrease of the DPV peak current (signal-off aptasensor) (Fig. 1C).

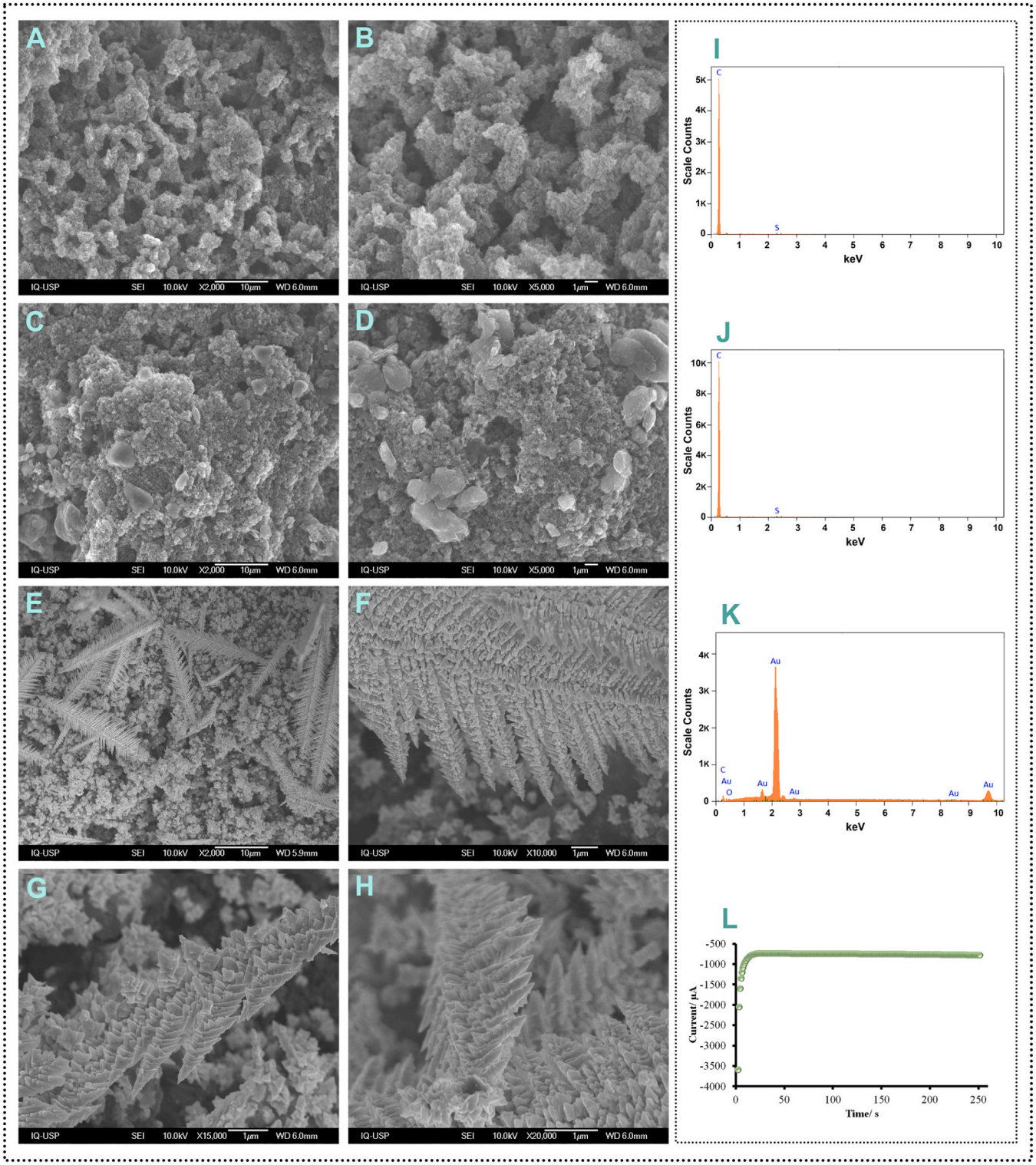

Fig. 2. FESEM micrographs of the bare 3D-printed electrode at a magnification of X2000 (A) and X5000 (B); modified electrode with GO at a magnification of X2000 (C) and X5000 (D); and modified electrode with GO/FGNCs at a magnification of X2000 (E), X10000 (F), X15000 (G), and X20000 (H); EDS analysis for the bare 3D-printed electrode (I), for the modified electrode with GO (J), and the modified electrode with GO/FGNCs (K); and the chronoamperogram related to electrodeposition of FGNCs on the electrode surface (deposition potential: 0 V and time: 250 s) (L).

3. Results and discussion

3.1. Characterizations of 3D-printed electrodes with different surfaces

3.1.1. Field emission scanning electron microscopy (FESEM), energy dispersive spectroscopy (EDS), and electrodeposition characterizations

FESEM analysis of the bare electrode surface with different magnifications showed a homogenous and regular distribution of carbon-based areas treated by CO_2 laser ablation (Fig. 2A and B). Porous carbon materials have a large surface area due to their intricate pore structure, and the bare electrode surface was susceptible to being modified with GO 2D sheets (Fig. 2C and D). The presence of several functional groups related to GO and improved structural integrity are some advantages of electrode surface modification with GO. Apparently, the porous areas of the electrode modified with GO decreased significantly (Fig. 2C and D), as if the electrode surface was coated with a thin and relatively uniform layer of GO sheets that could have partially penetrated, filled, and masked the underlying micropores of in the carbon substrate. The high electrical conductivity of GO also favored the subsequent modification by electrodeposition of FGNCs, for which

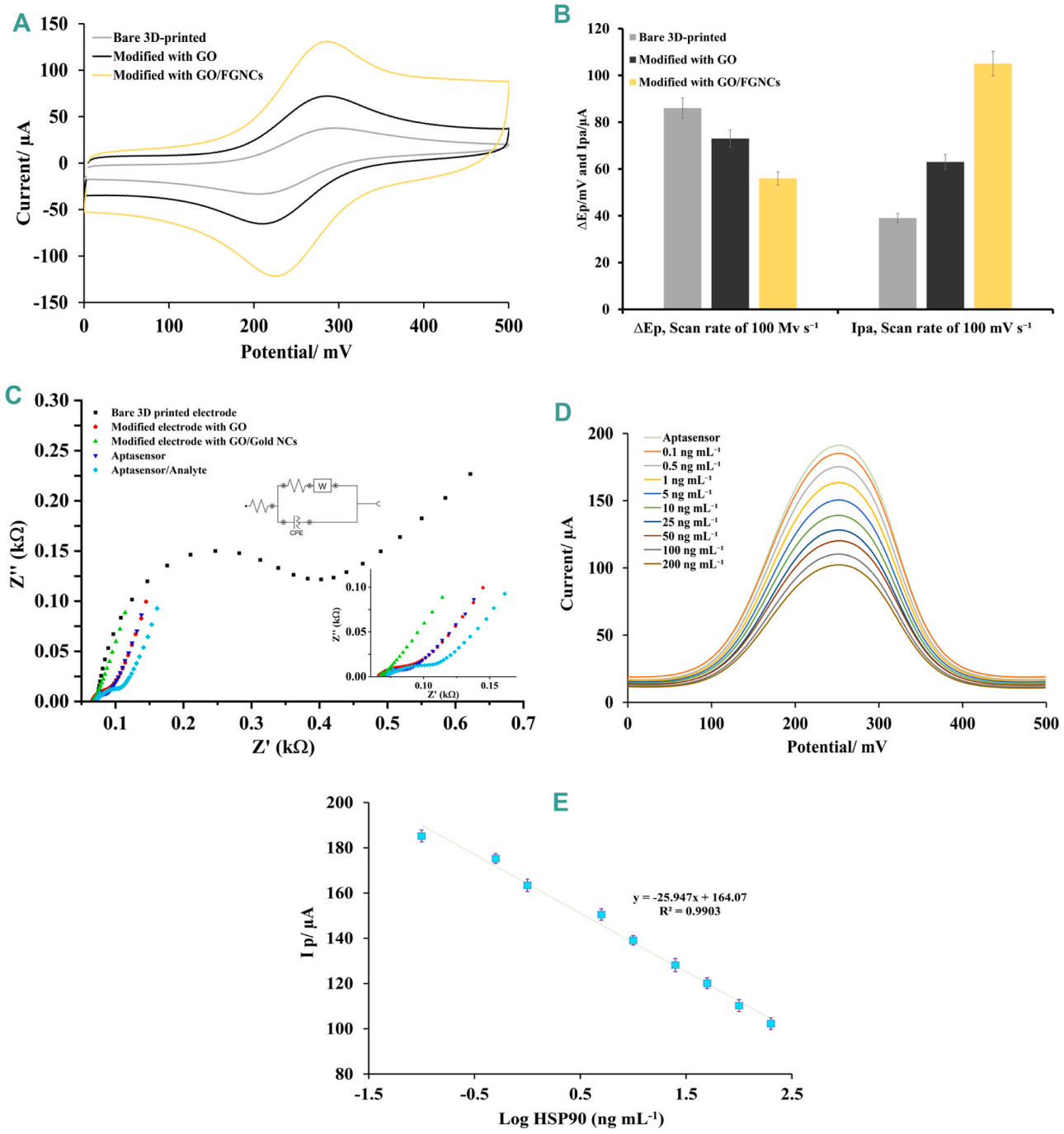

Fig. 3. CVs recorded in scan rate: 100 mV s^{-1} for three electrode surfaces (A); ΔE_p and $i_{p,a}$ obtained from CVs in the same condition (B); EIS results for three electrode surfaces and also for aptasensor and aptasensor bound with a typical concentration (10 ng mL^{-1}) of analyte; inset: EIS results in the absence of related data to the bare electrode and also the equivalent circuit most compatible with EIS data (C); DPVs recorded in the presence of different concentrations of HSP90 (D), and the calibration curve related to the logarithm of HSP90 concentrations (X-axis) and DPVs peak currents (Y-axis) (E); The error bars correspond to the SDs derived from three sets of repeated measurements (error bars: SD/ n=3).

surface micrographs were presented with different magnifications (Fig. 2E-H). The optimized electrodeposition conditions ([Au^{3+}]: 15 mM, potential: 0 V *vs.* Ag/AgCl and time: 250 s; Fig. 2L) and the presence of N, N-dimethylformamide (DMF) were the main reasons for growing of homogenous FGNCs on the electrode surface with mean width and length of approximately 65 nm and 509 nm, respectively (Fig. S4A, B). Using DMF improved the solubility of $HAuCl_4$ in the synthesis solution [58]. As a polar and stabilizing agent, DMF provided a homogeneous distribution of FGNCs on the electrode surface [59,60]. In addition, DMF acted as a structure-directing agent and influenced the growth, size, and morphology of synthesized gold nanoarray. The controlled synthesis, specific morphology, and homogenized distribution of FGNCs provided an optimum surface for interaction with thiol-functionalized aptamer strands (biorecognition element).

Fig. 2I, J, and K show the EDS analysis for different electrode surfaces (bare, modified with GO, and modified with GO/FGNCs). This assay was performed to characterize the chemical composition of materials for each electrode surface. In summary, Fig. 2I shows that the bare 3D-printed electrode was made mainly from carbon with weight of 98.8% and atom distribution of 99.6%. For the modified surface with GO, the EDS analysis presented in Fig. 2J, related values enhanced slightly (carbon weight of 99.3% and atom distribution of 99.8%.). In addition, the EDS analysis for the surface modified with GO/FGNCs showed that the gold weight and related atom distributions were 98.7% and 82.3%, respectively (Fig. 2K). In Table S3, more details about the EDS analysis are provided.

3.1.2. Electrochemical characterizations

The cyclic voltammograms (CVs) reversibility during the electron transfer at the electrode/solution interface was evaluated to estimate the advance in the electrochemically active area found after surface modifications mainly by CO_2 laser ablation, GO drop casting, and FGNCs electrodeposition. Scanning the circular area of printed conductive thermoplastic material with the laser promotes preferential thermal ablation of the polymer from the upper layers by the formation of volatile compounds, leaving behind and exposing much of the conductive carbon black and giving rise to the rough morphology as mentioned already (Fig. 2A and B). Typical CVs of the redox couple 0.5 mM [$Fe(CN)_6$]$^{4-}$/ 0.5 mM [$Fe(CN)_6$]$^{3-}$ in 0.5 M KCl electrolyte for a 3D-printed electrode activated by laser ablation presented well-developed anodic and cathodic waves whose peak potentials ($E_{p,a}$ *and* $E_{p,c}$) were separated by ΔE_p values increasing from circa 74–95 mV for scan rates (ν), rising from 2 to 200 mV s^{-1} in 12 increments, with an $E_{1/2}$ ($\approx E^{0'}$) remaining constant at 0.252±0.0014 V *vs.* Ag/Ag.Cl/KCl (3.5 M) (Figs. 3A-B and S5A). Drop casting of GO on the bare 3D-printed electrode and, even more so, electrodeposition of FGNCs improved the ΔE_p values and maintained the $E_{1/2}$ of 0.253±0.0035 V (n=36). For instance, CVs at ν of 100 mV s^{-1} presented ΔE_p of 86 mV, 73 mV, and 56 mV, respectively (Fig. 3A-B), for three electrode surface statuses, denoting a transition from a quasi-reversible to a reversible electrode process (at least up to 200 mV s^{-1}), once the expected ΔE_p for a reversible heterogeneous single electron transfer process is ≈57.5 mV (at 25°C, assuming linear semi-infinite diffusion) (Fig. S5A-C) [61].

The rate constants (k^0) of the [$Fe(CN)_6$]$^{4-/3-}$ redox process, involving the heterogeneous transfer of one electron, were estimated based on Nicholson's method. The required dimensionless kinetic parameter Ψ was calculated using the equation presented by Lavagnini et al. [62]. The mean k^0 values over the ν range of 100–200 mV s^{-1} (n = 5) were: 0.0089±0.0003, 0.013±0.003, and 0.056±0.018 cm s^{-1} respectively for three electrode surfaces in the order given before. The enhancement of k^0 reflects greater availability of active sites due to factors like the changeover from amorphous carbon to GO and to gold (FGNCs) as well as the increase in the electrochemically active area (as will be shown next), allowing fast enough electron transference to run the process under mass transport control, i.e., governed by diffusion of [$Fe(CN)_6$]$^{4-}$ and [$Fe(CN)_6$]$^{3-}$ to/from the electrode at least for $\nu \leq 200$ mV s^{-1}.

Here, a classical CV analysis was applied to the data based on the linearity and slopes of the anodic and cathodic peak currents ($i_{p,a}$ *and* $i_{p,c}$) against $\nu^{1/2}$. In agreement with the Randles-Ševčík equation [63], the anodic peak currents at 12 scan rates in the range from 2 to 200 mV s^{-1} resulted in straight lines *vs.* $\nu^{1/2}$ with nearly null intercept and R^2>0.995 (Fig. S5A-C), presenting the slopes of 3.76±0.05, 6.78±0.08, and 12.6 ±0.3 μA $mV^{-1/2}$ $s^{1/2}$ respectively for the bare, modified with GO and modified with GO/FGNCs electrodes. The linearity of the cathodic counterparts' plots was not the best ($R^2 \geq 0.990$), and the resulting $|i_{p,a}/-i_{p,c}|$ ratios were 1.14±0.04, 1.15±0.02, and 1.40±0.04 μA $mV^{-1/2}$ $s^{1/2}$, respectively. Considering the Randles-Ševčík equation and the geometrical (projected) area achieved from 3D-printed electrodes (⌀: 5 mm, 0.196 cm^2), the apparent electroactive surface areas for the bare, modified with GO, and GO/FGNCs electrodes were about 0.18, 0.31, and 0.50 cm^2, respectively. Using these areas and considering the redox probe concentration (1 mM), at ν of 100 mV s^{-1}, the mean current density for the three mentioned electrode surfaces was about 214 ±5 μA·cm^{-2}. Several other analyses were performed on CV data (including two more alternatives to estimate the electroactive surface area of the electrode), which have been presented and discussed in the Supplementary material and Figs. S5–6. In short, significant increases were found in the effective area of the 3D-printed electrodes after modification with GO and, even more, after electrodeposition of FGNCs, and, in comparison with conventional (expensive) solid gold disk electrodes polished with 1 μm abrasive, the accessible area for electroanalytical purposes, doubles, in rounded numbers. These comparative advantages are reinforced by the relative simplicity and quickness of the 3D printing, laser ablation, GO drop-casting, FGNCs electrodeposition for serial production, and low cost, with only 0.5 mg cm^{-2} of gold consumed.

The EIS analysis for all electrodes confirms that a loop in high frequencies occurred more intensely as components were added to the modified surfaces, suggesting that it might be associated with materials poorly adsorbed of the electrode surface being leached to the solution when a high-frequency oscillating potential is applied. As it affects both imaginary (Z") and real impedances (Z'), it can be associated with desorption processes affecting both double electric layer organization and the approximation of the electrochemical redox probe towards the electrode surface. The loops led to poorly adjusted equivalent circuits to the EIS spectra, and, therefore, we took a graphic analysis approach to provide a more accurate interpretation of the obtained spectra (Fig. 3C). The EIS spectrum obtained for the bare 3D-printed electrode within the range 100 kHz to 0.1 Hz present a semi-circle in high to mid-range frequencies that can be associated with the charge transfer resistance (RCT) of the electrochemical probe. Within that range, the Randles circuit associated in series with a CPE simulating the Warburg impedance presented good fitting with an estimated RCT = 277 Ω. However, for all modified electrodes, the very poorly defined or even absent semi-circle in the Nyquist plot evinces the electron charge transfer improvement by the surface modification with both GO and FGNCs which is corroborated by the log Z'(Ω) vs. log frequency (Hz) plot (Fig. 3C). As real impedance (Z') is associated with faradaic processes in the system, the modification with both GO and FGNCs suppress the drastic increase in the resistance values observed for the bare 3D-printed electrode curve associated with the semi-circle in the Nyquist plot, which means a drastic reduction in the RCT. This hypothesis is supported by the low phase angle magnitude of all modified electrodes compared to the bare 3D-printed electrode (Fig. S7A). In more detail, the phase angle shifts occur when the system reactance builds up once a capacitor is completely charged. In the electrochemical cell and before the phase angle shift, the only impedance observed within the system is the solution resistance (Rs). As frequency decreases, the increased time of the oscillating potential applied charges the electric double layer to its maximum value defined by its capacitance (Cdl). The results confirmed that once a capacitor, e.g., double electric layer, is fully charged, it generates an impedance (Z") to current flow, associated with a capacitor

reactance and exponentially increases. This growth is reflected by the increase in the phase angle magnitude and the appearance of a peak in the plot Z" vs. log frequency (Fig.S7B). In addition, other findings confirmed that once the imaginary impedance (Z") reaches half of the RCT value, the current starts to flow in phase as the phase angle decreases, and the real impedance starts to increase (Fig.S7C) [64].

Therefore, increased RCT values enhance the phase angle values up to 90° due to the slower transition of a capacitive behavior to a resistive behavior in the electrochemical system. When RCT is very low, the transition to the resistive behavior is fast as current freely flows in phase through the electrode surface. Here, the modified electrode with GO/FGNCs presented the fastest charge transfer as no phase angle shift was observed, and the resistance solution was the higher resistance through current flow in the system [64]. When the aptamer and analyte were added, there was a small increase in the phase angle shift, which can be associated with a small increase in charge transfer resistance and confirming the trapping of both aptamer and analyte on the electrode surface (Fig.S7D).

From that point, the diffusional mass transport limits the charge transfer at the electrode surface, and the electrode capacitance starts to become relevant as the |Z| in the Bode as *a* phase angle tends to 45° [64,65]. The same behavior was observed for the aptasensor and aptasensor bound with analyte statuses. In addition, the CVs obtained for the modified electrodes corroborate the hypothesis, as significant current increases were observed after modifications with GO and FGNCs.

3.2. Electroanalytical aptasensing of HSP90

The developed aptasensor was employed to detect various analyte concentrations, and results confirmed that this platform could detect the analyte linearly, ranging from 0.1 to 200 ng mL^{-1}. It should be noted that the optimum aptamer immobilization time on the electrode surface and the optimum time for binding with analyte molecules were determined in other experiments, with detailed procedures presented in the Supplementary Material and related results provided in Fig. S8A-C. Fig. 3D shows DPVs recorded in a three-electrode system (the modified electrode with GO/FGNCs as the working, a platinum wire as the counter, and an Ag/Ag.Cl as the reference electrodes) immersed in the electrolyte solution with the redox marker. The blank signal (aptasensor) DPV peak current was ~191 μA, and the DPV peak currents related to the minimum and maximum concentrations were 185.21 μA and 102.25 μA, respectively. Fig. 3E shows the calibration plot obtained from the relation between the logarithmic range of analyte concentrations versus DPV peak currents. The obtained linear regression was (Ip)/μA = - 25.95 log C HSP90 + 164.1, $R^2 = 0.990$, and the estimated LOD and LOQ were 0.1 ng mL^{-1} and 0.23 ng mL^{-1}, respectively. LOD was calculated based on 3σ/S and LOQ based on 10 σ/S (σ: standard deviation (SD) of aptasensor and S: slope of calibration plot) (S/N = 3).

Until now, biosensing platforms for detecting HSP90 have not developed significantly, and the literature presents just one electrochemical immunosensor for this biomarker [66]. In the cited study, an immunosensor was designed on a glassy carbon electrode modified with graphite-like g-C_3N_4-F127-Au nanosheets. Based on the interaction between Au and the amino group of the antibody, the immunosensor was established, and it could detect the analyte via linear sweep voltammetry in a linear range from 3.5 μg mL^{-1} to 2.43 mg mL^{-1} with a LOD of 2.67 μg mL^{-1} [66]. These limits were significantly improved in the present work.

3.3. Performance of HSP90 aptasensor

3.3.1. Repeatability

The repeatability of the aptasensor was evaluated by repeating the assembly of the aptasensor in the same condition five times. Hence, the first aptasensor was built, and related DPV was recorded. Then, to reset the surface, it was submerged in a piranha solution for 20 s, and all organic materials (aptamer and MCH) were removed. However, the outset layer of the electrode (modified surface with FGNCs) remained unchanged, and it was ready for the next aptamer immobilization. It should be noted that the presence of FGNCs also acted as a shielding agent against damaging GO sheets in interaction with the piranha solution. This cycle was repeated continuously in sequence, and the results showed that the DPVs peak current for five times assay was almost repeatable with RSD of about 1.20% (Figs. 4A and S9A).

3.3.2. Regeneration

This experiment was performed five times following the sequence: aptasensor preparation; DPV recording; bounding with the typical concentration of the analyte (10 ng mL^{-1}); DPV recording; debounding of the analyte by change of the conformation of aptamer strands during aptasensor immersion in hot water (95 °C for 5 min) [67]. The peak currents for the five couples of DPVs recorded after five cycles presented RSDs of 1.38% and 1.44%, respectively, for the bound and debound statuses, confirming a satisfactory performance (Figs. 4B and S9B).

3.3.3. Stability

The stability of the aptasensor was evaluated by an aptasensor bound with the typical concentration of the analyte (10 ng mL^{-1}), and its performance was monitored for 13 days. The assay was performed for days 1, 3, 5, 7, 10, 12, and 13. After recording each DPV, the aptasensor was refrigerated in a 20 mM tris(hydroxymethyl)aminomethane-HCl buffer, pH 7.4, for the following assays. The results showed that the DPVs peak current decrement for other days compared to the first day were 0.68%, 1.45%, 2.80%, 10.4%, 14.0%, and 21.0%, respectively (Fig. 4C and Fig. S9C). The aptasensor maintained almost the initial performance for one week (DPV peak current decrement: 2.8%, ΔI = 3.91 μA) with a negligible performance decrease.

3.3.4. Selectivity

This experiment was performed to analyze the selectivity performance of the aptasensor in the presence of several accessible proteins in biofluids, including HSP70, Hb, and HSA. In addition, the performance of the aptasensor was assessed in the presence of mixtures of mentioned interferences. Here, four aptasensors were prepared and exposed to concentrations of HSP90, including 0.1 ng mL^{-1} and 10 ng mL^{-1}, while the interferent concentrations were 0.1 ng mL^{-1} and 100 ng mL^{-1}. For the last group, mixtures of interferents were considered (mixture A: 10 ng mL^{-1} of all interferences, mixture B: 100 ng mL^{-1} of all interferences, and mixture C: 100 ng mL^{-1} of all interferences+10 ng mL^{-1} of HSP90). The ΔI values related to DPVs peak current used to present the effect of the interference compared to the blank signal (aptasensor), showing minimum ΔI (almost 0 μA (SD: 0.8 μA) for 0.1 ng mL^{-1} HSP70) and maximum ΔI (66.2 μA (SD: 2.7 μA) for mixture C). The minimum interfering effect of HSP70 may be due to different secondary structures of aptamer fits to detect this protein compared to the aptamer used for detecting HSP90 (Fig. S3 and recently developed HSP70 aptasensors [68,69]). It should be noted that the maximum ΔI found for mixture C (66.2 μA (SD: 2.7 μA)) was negligible compared to the ΔI found for 10 ng mL^{-1} HSP90 in this group (54.34 μA (SD: 0.96 μA)), confirming a selective aptasensing performance in detecting analyte molecules with high affinity (Figs. 4D and S10A-D).

3.3.5. Real sample application

The reliability application of aptasensor was evaluated for various concentrations of HSP90 spiked in six human serum samples (Table 1). The results showed that the found recovery RSD was about 7.3%, presenting an almost accurate assay for detecting the analyte in real serum samples.

4. Conclusion

Cancer monitoring using aptasensors is a perspective for developing

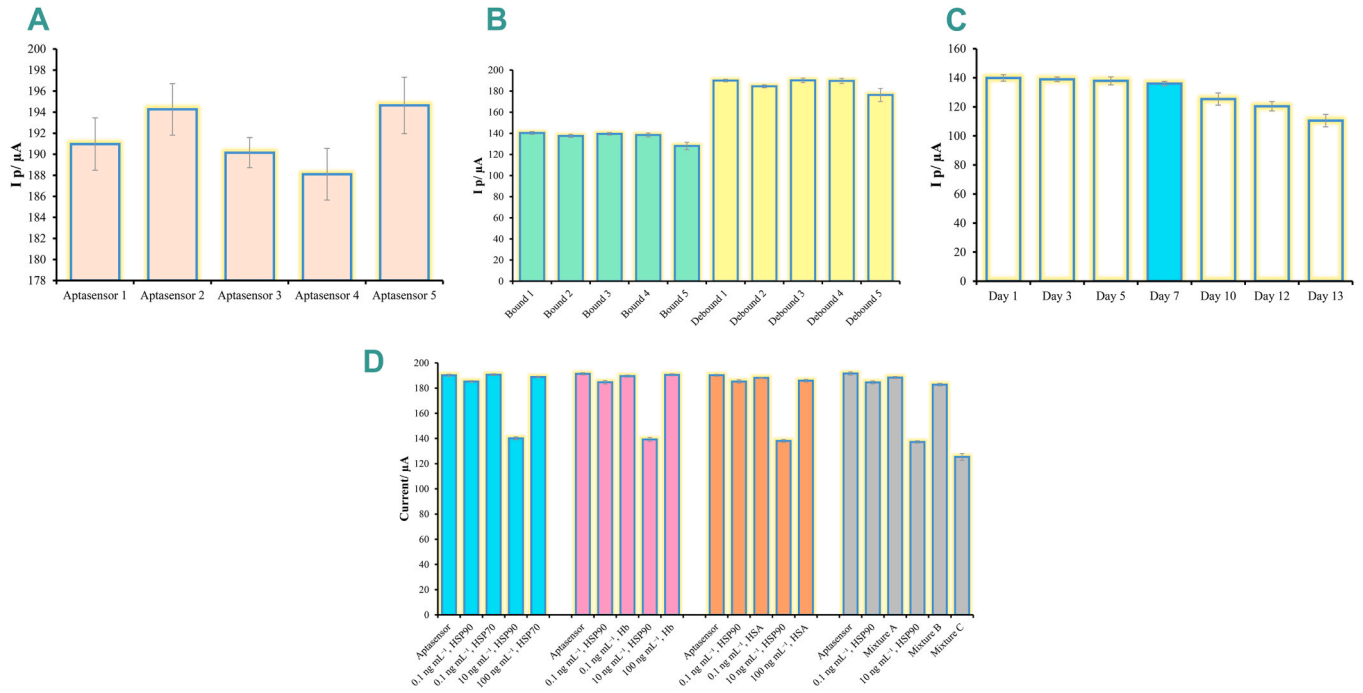

Fig. 4. Analysis of the performance of the aptasensor; repeatability of the performance for five sequential assemblies of the aptasensor on the same modified 3D-printed electrode (A); regeneration performance for aptasensor during five sequential cycles of bounding/deboundig for the typical concentration of HSP90 (B); stability of the aptasensor bound with the typical concentration of analyte for 13 days (seven assays) (C), and evaluation of the selectivity performance of aptasensor in the presence of analyte and several potential interferences (HSP70, Hb, HSA, and mixtures of analyte and/or interferences) with various concentrations (D); The error bars correspond to the SDs derived from three sets of repeated measurements (error bars: SD/ n=3).

Table 1
Recovery performance for spiked concentrations of HSP90 in serum samples (n=3).

Sample No.	*Added HSP90 (ng mL^{-1})*	*Detected HSP90 (ng mL^{-1})*	*Recovery (%)*
Serum 1	0.1	0.11±0.04	110
Serum 2	5	5.14±0.06	103
Serum 3	25	25.04±0.37	100
Serum 4	100	93.7±5.4	94
Serum 5	150	169±7.3	113
Serum 6	200	186±6.3	93

portable and accurate diagnostic tools. Optimized aptasensors can provide an accurate and rapid diagnosis by quantifying meager amounts of cancer biomarkers. Here, we designed and produced a 3D-printed electrode as a suitable substrate for hosting HSP90 aptamer strands after laser treatment and modifications with GO and FGNCs. This 3D-printed electrode has several advantages over other commercial electrodes and offers many options for surface treatments and modification, including CO_2 laser ablation, which is incompatible with commercial ones. In addition, minimizing the IR drops of voltage inside the 3D-printed electrode is a noteworthy achievement. Here, the device was designed with a copper wire path from the electrode to the external contact, featuring a much lower resistivity than any plausible track printed with CB-PLA. An additional advantage is the cost savings, with the cost of materials for producing each 3D-printed electrode estimated at less than US$ 0.10. The intended aptasensor by this electrode was able to provide a sensitive diagnosis with a wide detection range and a low LOD. Also, the performance of this aptasensor provided satisfactory figures of merit (reproducibility, regeneration, and stability). While this aptasensor showed satisfactory results, however, there are several shortcomings in this research. For example, ensuring the reproducibility of 3D-printed electrodes is always challenging due to optimizations in printing parameters and material properties. 3D-printed electrodes usually have rough surfaces, which may affect the electrochemical behaviors of the surface and make it difficult to calculate the exact electroactive surface area. Another issue should be noted: the HSP90 is not a specific cancer biomarker, but the determination of this biomarker can be helpful as a cancer biomarker. Future developments can consider reduced electrode size, producing some parts of the electrodes with other methods, modification with other nanomaterials, integration with biomolecular techniques, and development of more advanced biosensing platforms such as sandwich assembly.

CRediT authorship contribution statement

Masoud Negahdary: Conceptualization, Methodology, Formal analysis, Writing - Original Draft, Writing - Review & Editing. **Claudimir Lucio do Lago:** Methodology, Software, Data Curation, Writing - Review & Editing. **Ivano Gebhardt Rolf Gutz:** Formal analysis, Validation, Supervision, Writing - Review & Editing. **Rafael Martos Buoro:** Formal analysis, Writing - Review & Editing. **Michelangelo Durazzo:** Investigation. **Lúcio Angnes:** Funding acquisition, Resources, Supervision, Writing - Review & Editing.

Declaration of Competing Interest

The authors declare that they have no known competing financial interests or personal relationships that could have appeared to influence the work reported in this paper.

Data availability

Data will be made available on request.

Acknowledgements

The authors would like to thank the Sao Paulo Research Foundation-FAPESP (projects 2019/27021–4, 2018/08782–1, 2017/13137–5, and

2014/50867–3) and the National Council for Research-CNPq (processes 311847–2018–8, 302839/2020–8, 307259/2021–8, and 465389/2014–7). The authors are also appreciative to Central Analítica (IQ-USP), and Laboratório de Microscopia e Microanálise do Centro de Ciência e Tecnologia de Materiais do IPEN/CNEN-SP for material characterization facilities.

Appendix A. Supporting information

Supplementary data associated with this article can be found in the online version at doi:10.1016/j.snb.2024.135592.

References

1 D. Crosby, S. Bhatia, K.M. Brindle, L.M. Coussens, C. Dive, M. Emberton, et al., Early detection of cancer, Science 375 (6586) (2022) eaay9040.
2 R.C. Fitzgerald, A.C. Antoniou, L. Fruk, N. Rosenfeld, The future of early cancer detection, Nat. Med. 28 (4) (2022) 666–677.
3 G. Manasa, R.J. Mascarenhas, N.P. Shetti, S.J. Malode, T.M. Aminabhavi, Biomarkers for early diagnosis of ovarian carcinoma, ACS Biomater. Sci. Eng. 8 (7) (2022) 2726–2746.
4 J. Nayak, M.N. Favorskaya, S. Jain, B. Naik, M. Mishra (Eds.), Advanced Machine Learning Approaches in Cancer Prognosis: Challenges and Applications, Springer International Publishing,, 2021.
5 M. Pal, T. Muinao, H.P.D. Boruah, N. Mahindroo, Current advances in prognostic and diagnostic biomarkers for solid cancers: Detection techniques and future challenges, Biomed. Pharmacother. 146 (2022) 112488.
6 P. Johnson, Q. Zhou, D.Y. Dao, Y.D. Lo, Circulating biomarkers in the diagnosis and management of hepatocellular carcinoma, Nat. Rev. Gastroenterol. Hepatol. 19 (10) (2022) 670–681.
7 L.S. Kristensen, T. Jakobsen, H. Hager, J. Kjems, The emerging roles of circRNAs in cancer and oncology, Nat. Rev. Clin. Oncol. 19 (3) (2022) 188–206.
8 A.M. DeLouize, G. Eick, S.D. Karam, J.J. Snodgrass, Current and future applications of biomarkers in samples collected through minimally invasive methods for cancer medicine and population-based research, Am. J. Hum. Biol. 34 (11) (2022) e23665.
9 N. Ghaffari Laleh, M. Ligero, R. Perez-Lopez, J.N. Kather, Facts and hopes on the use of artificial intelligence for predictive immunotherapy biomarkers in cancer, Clin. Cancer Res. 29 (2) (2023) 316–323.
10 P. Song, L.R. Wu, Y.H. Yan, J.X. Zhang, T. Chu, L.N. Kwong, et al., Limitations and opportunities of technologies for the analysis of cell-free DNA in cancer diagnostics, Nat. Biomed. Eng. 6 (3) (2022) 232–245.
11 C. Hu, J. Yang, Z. Qi, H. Wu, B. Wang, F. Zou, et al., Heat shock proteins: Biological functions, pathological roles, and therapeutic opportunities, MedComm 3 (3) (2022) e161.
12 A.A.A. Asea, P. Kaur (Eds.), Heat Shock Protein 90 in Human Diseases and Disorders, Springer International Publishing,, 2019.
13 H. Javid, P. Hashemian, S. Yazdani, A. Sharbaf Mashhad, M. Karimi-Shahri, The role of heat shock proteins in metastatic colorectal cancer: A review, J. Cell. Biochem. 123 (11) (2022) 1704–1735.
14 Z. Fu, B. Jia, Advances in the role of heat shock protein 90 in prostate cancer, Andrologia 54 (4) (2022) e14376.
15 S.D. Ginsberg, S. Sharma, L. Norton, G. Chiosis, Targeting stressor-induced dysfunctions in protein–protein interaction networks via epichaperomes, Trends Pharmacol. Sci. 44 (1) (2023) 20–33.
16 M. Kielbik, I. Szulc-Kielbik, M. Klink, Calreticulin—multifunctional chaperone in immunogenic cell death: potential significance as a prognostic biomarker in ovarian cancer patients, Cells 10 (1) (2021) 130.
17 C.A. Basset, F. Rappa, R. Barone, A.M. Florena, R. Porcasi, E. Conway de Macario, et al., The chaperone system in salivary glands: Hsp90 prospects for differential diagnosis and treatment of malignant tumors, Int. J. Mol. Sci. 23 (16) (2022) 9317.
18 M. Wang, Z. Jiang, R. Liu, The diagnostic value of Hsp90? in monitoring treatment responses in lung cancer, Turk. J. Med. Sci. 52 (3) (2022) 747–753.
19 K. Su, Y. Liu, P. Wang, K. He, F. Wang, H. Chi, et al., Heat-shock protein 90α is a potential prognostic and predictive biomarker in hepatocellular carcinoma: a large-scale and multicenter study, Hepatol. Int. 16 (5) (2022) 1208–1219.
20 A. Hasan, S.F. Rizvi, S. Parveen, S.S. Mir, Heat shock proteins as biomarkers for early-stage diagnosis of lung cancer. In: Detection Systems in Lung Cancer and Imaging, Volume 1 [Internet], IOP Publishing,, 2022, https://doi.org/10.1088/978-0-7503-3355-9ch10.
21 F. Fontana, M. Anselmi, P. Limonta, Molecular Mechanisms of Cancer Drug Resistance: Emerging Biomarkers and Promising Targets to Overcome Tumor Progression, Cancers 14 (7) (2022) 1614.
22 W. Chen, G. Li, J. Peng, W. Dai, Q. Su, Y. He, Transcriptomic analysis reveals that heat shock protein 90α is a potential diagnostic and prognostic biomarker for cancer, Eur. J. Cancer Prev. 29 (4) (2019) 357–364.
23 S.-Y. Shin, M.M. Centenera, J.T. Hodgson, E.V. Nguyen, L.M. Butler, R.J. Daly, L. K. Nguyen, A Boolean-based machine learning framework identifies predictive biomarkers of HSP90-targeted therapy response in prostate cancer, Front. Mol. Biosci. 10 (2023) 1094321.
24 C. Duan, K. Li, X. Pan, Z. Wei, L. Xiao, Hsp90 is a potential risk factor for ovarian cancer prognosis: an evidence of a Chinese clinical center, BMC Cancer 23 (1) (2023) 489.
25 S. Saber, E.E. Abd El-Fattah, A.M. Abdelhamid, A.A. Mourad, M.A.M. Hamouda, A. Elrabat, et al., Innovative challenge for the inhibition of hepatocellular carcinoma progression by combined targeting of HSP90 and STAT3/HIF-1α signaling, Biomed. Pharmacother. 158 (2023) 114196.
26 W. Wei, M. Liu, S. Ning, J. Wei, J. Zhong, J. Li, et al., Diagnostic value of plasma HSP90α levels for detection of hepatocellular carcinoma, Bmc Cancer 20 (1) (2020) 9.
27 J. Niinimäki, H. Sihto, J. Arola, T. Vesterinen, HSP90 expression is associated with outcome in pulmonary carcinoid tumor patients, Transl. Lung Cancer Res. 12 (9) (2023) 1876.
28 S.J. Mishra, W. Liu, K. Beebe, M. Banerjee, C.N. Kent, V. Munthali, et al., The development of Hsp90β-selective inhibitors to overcome detriments associated with pan-Hsp90 inhibition, J. Med. Chem. 64 (3) (2021) 1545–1557.
29 M. Negahdary, Aptamers in nanostructure-based electrochemical biosensors for cardiac biomarkers and cancer biomarkers: A review, Biosens. Bioelectron. 152 (2020) 112018.
30 M. Negahdary, L. Angnes, Recent advances in electrochemical nanomaterial-based aptasensors for the detection of cancer biomarkers, Talanta 259 (2023) 124548.
31 M. Negahdary, A. Sharma, T.D. Anthopoulos, L. Angnes, Recent advances in electrochemical nanobiosensors for cardiac biomarkers, TrAC Trends Anal. Chem. 164 (2023) 117104.
32 A. Atapour, H. Khajehzadeh, M. Shafie, M. Abbasi, S. Mosleh-Shirazi, S.R. Kasaee, A. M. Amani, Gold nanoparticle-based aptasensors: A promising perspective for early-stage detection of cancer biomarkers, Mater. Today Commun. 30 (2022) 103181.
33 A. Villalonga, B. Mayol, R. Villalonga, D. Vilela, Electrochemical aptasensors for clinical diagnosis. A review of the last five years, Sens. Actuators B: Chem. (2022) 132318.
34 Shraim AaS, Abdel Majeed, B.A. Al-Binni, M.A. Hunaiti, A. Therapeutic, Potential of Aptamer–Protein Interactions. ACS Pharmacology & Translational, Science 5 (12) (2022) 1211–1227.
35 K.Y. Chan, A.B. Kinghorn, M. Hollenstein, J.A. Tanner, Chemical modifications for a next generation of nucleic acid aptamers, ChemBioChem 23 (15) (2022) e202200006.
36 Y. Dong (Ed.), Aptamers for Medical Applications: From Diagnosis to Therapeutics, Springer Nature,, Singapore, 2021.
37 M. Negahdary, L. Angnes, Application of electrochemical biosensors for the detection of microRNAs (miRNAs) related to cancer, Coord. Chem. Rev. 464 (2022) 214565.
38 M. Negahdary, M. Behjati-Ardakani, N. Sattarahmady, H. Yadegari, H. Heli, Electrochemical aptasensing of human cardiac troponin I based on an array of gold nanodumbbells-Applied to early detection of myocardial infarction, Sens. Actuators B: Chem. 252 (2017) 62–71.
39 M. Negahdary, W.B. Veloso, R.P. Bacil, R.M. Buoro, I.G.R. Gutz, T.R.L.C. Paixão, et al., Aptasensing of beta-amyloid (Aβ(1−42)) by a 3D-printed platform integrated with leaf-shaped gold nanodendrites, Sens. Actuators B: Chem. 393 (2023) 134130.
40 K. Zub, S. Hoeppener, U.S. Schubert, Inkjet printing and 3D printing strategies for biosensing, analytical, and diagnostic applications, Adv. Mater. 34 (31) (2022) 2105015.
41 D. Calabria, E. Lazzarini, A. Pace, I. Trozzi, M. Zangheri, S. Cinti, et al., Smartphone-based 3D-printed electrochemiluminescence enzyme biosensor for reagentless glucose quantification in real matrices, Biosens. Bioelectron. 227 (2023) 115146.
42 A. Keirouz, Y.L. Mustafa, J.G. Turner, E. Lay, U. Jungwirth, F. Marken, H.S. Leese, Conductive Polymer-Coated 3D Printed Microneedles: Biocompatible Platforms for Minimally Invasive Biosensing Interfaces, Small 19 (14) (2023) 2206301.
43 J.S. Stefano, C. Kalinke, R.G. da Rocha, D.P. Rocha, V.A.O.P. da Silva, J.A. Bonacin, et al., Electrochemical (bio) sensors enabled by fused deposition modeling-based 3D printing: A guide to selecting designs, printing parameters, and post-treatment protocols, ACS Publ. (2022).
44 U. Detamornrat, E. McAlister, A.R. Hutton, E. Larrañeta, R.F. Donnelly, The role of 3D printing technology in microengineering of microneedles, Small 18 (18) (2022) 2106392.
45 A.K.K. Padinjareveetil, M. Pumera, Advances in Designing 3D-Printed Systems for CO_2 Reduction, Adv. Mater. Interfaces 10 (8) (2023) 2201734.
46 R.M. Cardoso, D.M.H. Mendonça, W.P. Silva, M.N.T. Silva, E. Nossol, R.A.B. da Silva, et al., 3D printing for electroanalysis: From multiuse electrochemical cells to sensors, Anal. Chim. Acta 1033 (2018) 49–57.
47 R.M. Cardoso, C. Kalinke, R.G. Rocha, P.L. dos Santos, D.P. Rocha, P.R. Oliveira, et al., Additive-manufactured (3D-printed) electrochemical sensors: A critical review, Anal. Chim. Acta 1118 (2020) 73–91.
48 J.F.S. Pereira, R.G. Rocha, S.V.F. Castro, A.F. João, P.H.S. Borges, D.P. Rocha, et al., Reactive oxygen plasma treatment of 3D-printed carbon electrodes towards high-performance electrochemical sensors, Sens. Actuators B: Chem. 347 (2021) 130651.
49 L.R. Silva, A. Gevaerd, L.H. Marcolino-Junior, M.F. Bergamini, T.A. Silva, B. C. Janegitz, 3D-printed electrochemical devices for sensing and biosensing of biomarkers. Advances in Bioelectrochemistry Volume 2: Biomimetic, Bioelectrocatalysis and Materials Interfaces, Springer,, 2022, pp. 121–136.
50 H. Jiang, Z. Sun, C. Zhang, X. Weng, 3D-architectured aptasensor for ultrasensitive electrochemical detection of norovirus based on phosphorene-gold nanocomposites, Sens. Actuators B: Chem. 354 (2022) 131232.
51 W.B. Veloso, T.R.L.C. Paixão, G.N. Meloni, 3D printed electrodes design and voltammetric response, Electrochim. Acta 449 (2023) 142166.
52 B. Hüner, N. Demir, M.F. Kaya, Ni-Pt coating on graphene based 3D printed electrodes for hydrogen evolution reactions in alkaline media, Fuel 331 (2023) 125971.
53 M. Negahdary, Electrochemical aptasensors based on the gold nanostructures, Talanta 216 (2020) 120999.

54 R. Eivazzadeh-Keihan, E.B. Noruzi, E. Chidar, M. Jafari, F. Davoodi, A. Kashtiaray, et al., Applications of carbon-based conductive nanomaterials in biosensors, Chem. Eng. J. 442 (2022) 136183.
55 W.B. Veloso, V.N. Ataide, D.P. Rocha, H.P. Nogueira, A. de Siervo, L. Angnes, et al., 3D-printed sensor decorated with nanomaterials by CO_2 laser ablation and electrochemical treatment for non-enzymatic tyrosine detection, Microchim. Acta 190 (2) (2023) 63.
56 J.J. Rossi, S. Yoon, N. Habib, Bi-specific aptamer, Google Pat. (2022). US11219635B2.
57 H. Du, T. Yin, J. Wang, G. Jie, Multifunctional Photoelectrochemical Biosensor Based on ZnIn2S4/ZnS QDs@ Au–Ag-Reversed Photocurrent of Cu-Metal–Organic Framework Coupled with CRISPR/Cas-12a-Shearing for Assay of Dual Targets, Anal. Chem. 95 (17) (2023) 7053–7061.
58 I. Pastoriza-Santos, L.M. Liz-Marzán, N,N-Dimethylformamide as a Reaction Medium for Metal Nanoparticle Synthesis, Adv. Funct. Mater. 19 (5) (2009) 679–688.
59 Majid M. Heravi, M. Ghavidel, L. Mohammadkhani, Beyond a solvent: triple roles of dimethylformamide in organic chemistry, RSC Adv. 8 (49) (2018) 27832–27862.
60 J. Zhou, J. Ralston, R. Sedev, D.A. Beattie, Functionalized gold nanoparticles: synthesis, structure and colloid stability, J. Colloid Interface Sci. 331 (2) (2009) 251–262.
61 M.G. Trachioti, A.C. Lazanas, M.I. Prodromidis, Shedding light on the calculation of electrode electroactive area and heterogeneous electron transfer rate constants at graphite screen-printed electrodes, Microchim. Acta 190 (7) (2023) 251.
62 I. Lavagnini, R. Antiochia, F. Magno, An extended method for the practical evaluation of the standard rate constant from cyclic voltammetric data, Electroanal.: Int. J. Devoted Fundam. Pract. Asp. Electroanal. 16 (6) (2004) 505–506.
63 A.J. Bard, L.R. Faulkner, Electrochemical Methods: Fundamentals and Applications, Wiley,, 2000.
64 M.E. Orazem, B. Tribollet, Electrochemical impedance spectroscopy, N. Jersey 1 (2008) 383–389.
65 N.O. Laschuk, E.B. Easton, O.V. Zenkina, Reducing the resistance for the use of electrochemical impedance spectroscopy analysis in materials chemistry, RSC Adv. 11 (45) (2021) 27925–27936.
66 C. Sun, M. Zhang, Q. Fei, D. Wang, Z. Sun, Z. Geng, et al., Graphite-like g-C3N4-F127-Au nanosheets used for sensitive monitoring of heat shock protein 90, Sens. Actuators B: Chem. 256 (2018) 160–166.
67 K.M. Cheung, K.-A. Yang, N. Nakatsuka, C. Zhao, M. Ye, M.E. Jung, et al., Phenylalanine Monitoring via Aptamer-Field-Effect Transistor Sensors, ACS Sens. 4 (12) (2019) 3308–3317.
68 M. Negahdary, M.H. Hirata, S.K. Sakata, R.M. Ciconelli, G.M. Bastos, J.B. Borges, et al., Sandwich-like electrochemical aptasensing of heat shock protein 70 kDa (HSP70): Application in diagnosis/prognosis of coronavirus disease 2019 (COVID-19), Anal. Chim. Acta 1242 (2023) 340716.
69 M. Negahdary, L. Angnes, An aptasensing platform for detection of heat shock protein 70 kDa (HSP70) using a modified gold electrode with lady fern-like gold (LFG) nanostructure, Talanta 246 (2022) 123511.

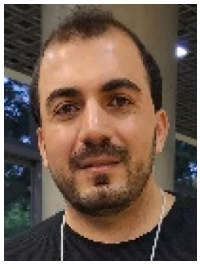

Masoud Negahdary is a postdoctoral researcher at Department of Biomedical Engineering, Texas A&M University, College Station, USA. He was a postdoctoral researcher at the Institute of Chemistry, University of São Paulo (USP), Brazil (2021-December 2023). He received his Ph.D. (Clinical Biochemistry) from Yazd University of Medical Sciences, Iran (2018). His doctoral thesis and other main biosensing research were performed at the Nanomedicine and Nanobiology Research Center, Shiraz University of Medical Sciences, Iran (2015–2019).

Claudimir Lucio do Lago is a full professor at the Institute of Chemistry, University of São Paulo (Brazil). His areas of interest include the development of instrumentation and analytical methods with an emphasis on capillary electrophoresis. He has published over 120 scientific articles, as well as chapters in books. He is a member of the editorial board of the Hardware journal.

Ivano G. R. Gutz received his Ph.D. in analytical chemistry in 1978 at the University of São Paulo, where he is full professor at the Institute of Chemistry since 1992. His research interests include electroanalytical chemistry, analytical instrumentation and automation.

Rafael Martos Buoro Obtained his Ph.D. in 2014 at the University of São Paulo under the supervision of Prof. Silvia Helena Pires Serrano with one year abroad period under the supervision of Prof. Ana Maria Oliveira Brett at FCTUC – Universidade de Coimbra in 2013. He is a Professor at the Departamento de Química e Física Molecular – IQSC – Universidade de São Paulo since 2016.

Michelangelo Durazzo Is a researcher at IPEN in Materials Engineering with a focus on nuclear materials. Specialized in the physical characterization of materials, including scanning electron microscopy, optical microscopy, image analysis, X-ray diffraction, and thermal analysis; also a professor in the Nuclear Technology program at the University of São Paulo, USP/PEN.

Lúcio Angnes is a full professor at the Institute of Chemistry of the University of Sao Paulo. His research interests include the construction of electrodes with new and alternative materials, development of modified electrodes, arrays of microelectrodes, the design of different procedures of aptamer immobilization, and association of the created devices with bioanalysis systems. He is a member of the Sao Paulo State Academy of Science.